atoms

MDPI

*Article*

# Calculation of Energy and Angular Distributions of Electrons Produced in Intermediate-Energy p + $H_2$ Collisions

**Corey T. Plowman [1], Kade H. Spicer [1] and Alisher S. Kadyrov [1,2,*]**

[1] Department of Physics and Astronomy, Curtin University, P.O. Box U1987, Perth, WA 6845, Australia
[2] Institute of Nuclear Physics, Ulugbek, Tashkent 100214, Uzbekistan
* Correspondence: a.kadyrov@curtin.edu.au

**Abstract:** We extend the two-centre wave-packet convergent close-coupling approach to doubly differential ionisation in proton collisions with $H_2$ to intermediate projectile energies. The results for the doubly differential cross section at projectile energies from 48 to 200 keV are presented as a function of the energy and angle of emitted electrons. We consider a wide range of emission angles from 10 to 160°, and compare our results to experimental data, where available. Excellent agreement between the presented results and the experimental data was found, especially for emission angles less than 130°. For very large backward emission angles our calculations tended to slightly overestimate the experimental data when energetic electrons are ejected and the doubly differential cross section is very small. This discrepancy may be due to the large uncertainties in the experimental data in this region and the model target description. Overall, the present results show significant improvement upon currently available theoretical results and provide a consistently accurate description of this process across a wide range of incident energies.

**Keywords:** ion-atom collisions; ion-molecule collisions; proton; molecular hydrogen; ionisation; capture into continuum



**Citation:** Plowman, C.T.; Spicer, K.H.; Kadyrov, A.S. Calculation of Energy and Angular Distributions of Electrons Produced in Intermediate-Energy p + $H_2$ Collisions. *Atoms* **2023**, *11*, 112. https://doi.org/10.3390/atoms11080112

Academic Editors: Jean-Christophe Pain, Michael Schulz and Karoly Tokesi

Received: 8 July 2023
Revised: 9 August 2023
Accepted: 10 August 2023
Published: 14 August 2023



## 1. Introduction

One of the most fundamental processes in nature is the scattering of charged particles off an atom or molecule. Atomic scattering occurs throughout the universe, from nuclear fusion, that powers stars, to hadron therapy for cancer, that uses ions to destroy deep-seated tumours [1,2]. For this reason, detailed studies of the underlying principles of ion–atom collisions remain an active area of research [3,4]. It is well known that, on the energy scale where these collisions occur, their dynamics is governed by quantum mechanics. A wave function satisfying Schrödinger's equation of motion defines the development of the state of the particles through space and time. While the solutions to the Schrödinger equation of the hydrogen atom are analytically known, adding additional particles significantly complicates the problem so that exact solution is no longer possible. This makes scattering of another particle on a quantum-mechanical few-body system extremely complicated to model.

Significant differences still exist between theory and experiment for some of the most fundamental collision systems. In particular, calculation of the fully differential ionisation cross section remains a challenging problem. For example, the state-of-the-art quantum-mechanical convergent close-coupling approach to $C^{6+}$ + He collisions [5] resulted in differences in the features of the fully differential emission when compared to the three-dimensional pattern experimentally observed by Schulz et al. [6]. These calculations were performed in the high-energy regime where electron capture is believed to play a negligible role in the collision dynamics, significantly simplifying the theoretical problem. Currently available calculations of the doubly and triply differential cross sections for ionisation in p + $H_2$ collisions also show inconsistent agreement with experimental measurements; see,

for instance, refs. [7–9]. Our ultimate goal was to address these discrepancies using the two-centre formulation of the wave-packet convergent close-coupling (WP-CCC) method that includes strong coupling effects between various reaction channels.

In this work we focus on the energy and angular distributions of electrons produced in proton collisions with molecular hydrogen. This system represents one of the most fundamental ion–molecule collision systems and describing this scattering process accurately is a key step towards developing theories for calculating ion scattering on more complex targets, such as water and other molecules of biological relevance. Accurate theories for calculating stopping power cross sections for such molecules are urgently required for Monte-Carlo simulation for treatment planning in hadron therapy [1,10]. For proton collisions with $H_2$, the ionisation cross section has a maximum around a projectile energy of 70 keV and becomes the dominant energy loss mechanism at higher incident energies. This makes calculations particularly difficult in this region since there are many competing processes that can occur as a result of scattering, and reaction channels are strongly coupled to each other. Additionally, the ionisation cross section differential, in both the energy and emission angle of the ejected electrons, provides a more thorough description of the outcome of scattering than the total or singly differential cross sections could do. For that reason, calculating the doubly differential cross section represents a more stringent test on theory.

Experimentally, $p + H_2$ collisions are easier to investigate than the (theoretically simpler) $p + H$ system due to the difficulties in preparing atomic hydrogen target atoms [11]. As a result, the molecular target has been experimentally studied extensively [12,13]. The angular and energy distributions of ejected electrons were first measured simultaneously by Kuyatt and Jorgensen [14] across an incident energy range from 50 to 100 keV. Later, it was discovered that their low-energy data near the ionisation threshold was not accurate due to inefficiencies in the apparatus [11]. Disagreement between their data and the first-order Born approximation (FBA) calculations available at the time prompted further investigations into this process. Rudd and Jorgensen [15] measured the doubly differential cross section for ionisation at 100 keV over a wider range of ejected-electron energies and angles. They also concluded that although the energy distribution of the ejected electrons was represented reasonably by the FBA calculations, agreement between theory and experiment for the angular distribution was very poor. They extended their measurements to an incident energy of 300 keV [16] where the measured total ionisation cross section demonstrated improved agreement with the FBA one. However, significant disagreement was still observed between theory and experiment for the doubly differential cross section for ionisation. Additionally, when the differential cross sections measured in these early experiments were integrated the resulting total ionisation cross section (TICS) was 35–100% larger than reported by direct measurements. Toburen and Wilson [17] measured the doubly differential cross section for ionisation in $p + H_2$ collisions from 300 keV up to 1.5 MeV. They reported an uncertainty of 25% for their measurements of low-energy electrons and, in general, their results agreed well with those of Rudd et al. [16] at 300 keV. However, their data deviated from that of Rudd et al. [16] at ejection energies less than 50 eV for ejection angles greater than 30°. The most significant difference was seen at the highest measured ejection energies and for emission in the backward direction, where the cross sections were very small and the signal to noise ratio in their measurements was low. They found that the first Born approximation agreed well with their measured doubly differential cross section (DDCS) for ionisation as a function of ejection energy only if the long-range electron–proton interaction was included. At the larger impact energies considered by Toburen and Wilson [17], the binary-encounter peak becomes visible for ejection of high-energy electrons at small emission angles. This secondary peak in the DDCS is the result of essentially binary collisions between the projectile and active electron. While binary-encounter theories based on this classical collision model have been developed, they cannot be applied to cross sections that are differential in the angle of emission. This is due to the fact that these cross sections are sensitive to the presence of the target nucleus, which

is ignored in the binary-encounter theories. Thus, these types of approaches have been confined to calculation of the total cross section and the singly differential cross section as a function of the ejected electron energy. The DDCS for ionisation was also measured by Gibson and Reid [18] at 50 keV over a range of ejection energies from 5 to 150 eV and angles from 0 to 100°. However, the TICS found that integrating their results differed from direct measurements by 33%. More recent experiments called into question the accuracy of their results due to potential spreading of their proton beam [19]. The greatest difficulty in obtaining accurate integrated cross sections for ionisation from measured DDCSs is the accuracy of the cross section data for very low energy electrons. This is where the DDCS is largest. Experiments can only measure to a finite minimum ejection energy, typically around 5 eV, and the value of the DDCS from this point to threshold must be estimated. The latest, and possibly, most accurate experimental measurements of this type were performed by Gealy et al. [11] for incident protons with energies from 20 to 114 keV. They reported the DDCS for ionisation as a function of both ejection energy and angle from electron energies as small as 1.5 eV to 400 eV at the highest incident energy. Their angular range extended from 15 to 165°. This experiment used a new apparatus specifically designed to measure the flux of low-energy ejected electrons accurately. Furthermore, the integrated cross sections in this work agreed well with independently measured total ionisation cross sections for the $p + H_2$ collision system.

Calculating the doubly differential cross section for ionisation as a function of ejected electron energy and emission angle in $p + H_2$ collisions has proven to be a significant challenge for theorists. There are only a few attempts to calculate this cross section available in the literature. Moreover, the majority of calculations have used the FBA that is only applicable at high projectile energies. Additionally, scattering on the molecular hydrogen target is often treated with either the so-called Bragg additivity rule or an energy-scaling procedure. Both of these approaches begin by calculating cross sections for scattering on atomic hydrogen. Then, results for the $H_2$ target are obtained by multiplying by a factor of 2, or applying the energy-scaling approach suggested in refs. [20,21]. The inability of these approaches to accurately model the underlying physics was demonstrated by the poor agreement with the experimental data of refs. [14–17]. A different approach was taken by Macek [22], that used the first term in the Neuman expansion of Faddeev's equations for the final state of the projectile-electron-residual ion system to calculate the DDCS for ionisation. The calculations were performed at an incident energy of 300 keV. The results showed improved agreement with the measured cross section compared to FBA calculations but still demonstrated significant deviation from the experimental data. In particular, the results of Macek [22] significantly overestimate the cross section near small ejection energies. This is possibly due to the fact that the Faddeev equation approach is not valid for breakup in a system of three charged particles. In this case, the kernel of the Faddeev equations becomes non-compact. The doubly differential cross section for ionisation as a function of ejected electron energy and angle were calculated by Galassi et al. [23], using both the FBA and the continuum distorted wave–eikonal initial state (CDW–EIS) method. As with the FBA, the CDW–EIS is a perturbative approach and only applicable at sufficiently high impact energies. Two methods for determining the cross section for the $H_2$ target were used. The first one is based on the simple Bragg additivity rule, which multiplies the CDW–EIS results for $p + H$ scattering by a factor of 2. The second one treats the target as two independent H atoms separated by the equilibrium inter-nuclear distance of the $H_2$ molecule. The cross section for proton scattering on $H_2$ is then given by the integral over all orientations of the product of the square of the magnitude of the amplitude for scattering on an effective atomic hydrogen target and an orientation-dependent factor resulting from the two scattering centres. The authors refer to the latter method as the continuum distorted wave–eikonal initial state–orbital (CDW–EIS–MO) method. Both approaches are compared to the experimental results of Gealy et al. [11] at 114 keV as a function of ejected electron energy at four different ejection angles. Their results show that Bragg's additivity rule is inadequate at providing accurate doubly differential cross

section for ionisation, overestimating the results of ref. [11], particularly for ejection at angles greater than 90°. Nevertheless, overall, the CDW–EIS–MO calculations demonstrate improved agreement with experiment.

Recently, we applied the two-centre wave-packet convergent close-coupling approach to calculate the energy and angular distribution of electrons emitted in collisions of 300-keV protons with $H_2$ [24], providing the most accurate theoretical description of this process to-date. The results demonstrated excellent agreement with the experimental data of Rudd et al. [16] and Toburen and Wilson [17]. Here, we provide details of the method and extend the calculations to more challenging lower incident energies, where the speed of the projectile is comparable to that of the target electrons. Specifically, we present the results at seven different projectile energies from 48 to 200 keV. In addition, we provide full details of the approach.

The layout of this paper is as follows. First, we provide a detailed review of the relevant literature. Then, we describe the presented method and give details of the calculations. Next, we present our results and provide a detailed discussion in the context of the experimental and theoretical data presently available in the literature. Unless specified otherwise, atomic unit (a.u.) is used throughout this manuscript.

## 2. Two-Centre Wave-Packet Convergent Close-Coupling Method

The WP-CCC method was first introduced to calculate differential cross sections for ionisation in antiproton collisions with atomic hydrogen [25]. Since then, it has been extended to tackle the differential ionisation problem in systems with positively charged projectiles [26–28] and more complex targets, such as helium [29] and molecular hydrogen [30]. Singly differential cross sections for direct scattering, electron capture, and ionisation have been thoroughly investigated for the following: $p + H$ collisions by Plowman et al. [28]; $p + He$ collisions by Spicer et al. [29,31]; and $p + H_2$ by Plowman et al. [30]. For $p + H$ collisions, doubly differential cross sections, as a function of both the ejected electron energy and projectile scattering angle, were presented by Abdurakhmanov et al. [27] at 75 keV. Here, we calculate the doubly differential cross section for ionisation in proton scattering on $H_2$ as a function of the ejected electron energy and emission angle. The underlying approach for calculating differential cross sections for ionisation in $p + H_2$ collisions is detailed in ref. [30]. The effective one-electron target structure of the $H_2$ molecule, as used in the WP-CCC approach, is described in ref. [32]. Here, we give a brief overview of the most relevant aspects of the theory.

### *2.1. Close-Coupling Formalism*

We consider proton collisions with $H_2$. In this work, we describe the molecular target using an effective one-electron treatment. The Schrödinger equation for the total scattering wave function $\Psi_i^+$, subject to the outgoing-wave boundary conditions, is written as

$$(H - E)\Psi_i^+ = 0, \tag{1}$$

where $H$ is the full three-body Hamiltonian of the collision system and $E$ is the total energy. Subscript $i$ refers to the initial channel, from which the total scattering wave develops, here, $i = 1$, representing the target in the ground electronic state in the initial channel. The total Hamiltonian for the scattering system is given by the sum of the free three-particle Hamiltonian of the projectile nucleus, target nucleus, and active electron, $H_0$, and the interaction between them, $V$,

$$H = H_0 + V. \tag{2}$$

The free-particle Hamiltonian is equivalently given by

$$H_0 = -\frac{1}{2\mu_T}\nabla_\rho^2 - \frac{1}{2}\nabla_{r_T}^2 \tag{3}$$

and

$$H_0 = -\frac{1}{2\mu_P}\nabla_\sigma^2 - \frac{1}{2}\nabla_{r_P}^2, \tag{4}$$

in the target and projectile coordinate systems, respectively. The reduced mass of the $p + H_2$ system is $\mu_T$, and the reduced mass of the $H + H_2{}^+$ system is $\mu_P$. We use two sets of Jacobi coordinates. In the first set, $\boldsymbol{r}_T$ is the position vector of the active electron relative to the target nucleus and $\boldsymbol{\rho}$ is the position of the projectile nucleus relative to the target system. In the second set, $\boldsymbol{r}_P$ is the position of the active electron relative to the projectile and $\boldsymbol{\sigma}$ is the position of the atom formed by the projectile after capturing the electron (hereafter called the projectile atom) relative to the residual target ion, $H_2^+$. The interaction potential is the sum of the inter-nuclear interaction and the potential between the active electron and each of the nuclei,

$$V = V_{\text{mod}}(R) - V_{\text{mod}}(r_T) - \frac{1}{r_P}. \tag{5}$$

In the effective one-electron treatment of $H_2$, the field of the residual target ion is collectively represented using the model effective potential proposed in ref. [33]. Parameters of the potential are chosen to ensure the ionisation energy of the target corresponds to the ionisation energy of $H_2$ at the equilibrium inter-nuclear distance. For a more detailed discussion of the target description, see Plowman et al. [32].

The total scattering wave function in Equation (1) is expanded, in terms of $N$ target-centred ($\psi_\alpha^T$) and $M$ projectile-centred ($\psi_\beta^P$) pseudo-states,

$$\Psi_i^+ \approx \sum_{\alpha=1}^{N} F_\alpha(t,\boldsymbol{b})\psi_\alpha^T(\boldsymbol{r}_T)e^{i\boldsymbol{q}_\alpha\cdot\boldsymbol{\rho}} + \sum_{\beta=1}^{M} G_\beta(t,\boldsymbol{b})\psi_\beta^P(\boldsymbol{r}_P)e^{i\boldsymbol{q}_\beta\cdot\boldsymbol{\sigma}}, \tag{6}$$

where $F_\alpha(t,\boldsymbol{b})$ and $G_\beta(t,\boldsymbol{b})$ are expansion coefficients that depend on time $t$ and impact parameter $\boldsymbol{b}$. The momentum of the projectile, relative to the target, is denoted $\boldsymbol{q}_\alpha$, and the momentum of the projectile atom relative to the target nucleus is denoted by $\boldsymbol{q}_\beta$. In other words, we position the origin of the coordinate system at the target nucleus. The projectile moves with velocity $\boldsymbol{v}$ in a straight line parallel to the $z$-axis with its position given by $\boldsymbol{R} = \boldsymbol{b} + \boldsymbol{v}t$, where the impact parameter is perpendicular to the projectile velocity, $\boldsymbol{b}\cdot\boldsymbol{v} = 0$. We include both target- and projectile-centred basis states in Equation (6) to accurately calculate ionisation, since the positive charge of the projectile results in a high probability of ejected electrons leaving the system in the vicinity of the projectile nucleus. This electron capture into the continuum process contributes significantly to the total ionisation cross section [28]. While single-centre methods can, in principle, calculate ionisation processes in collisions of positively charged projectiles, in practice, a prohibitively large number of continuum pseudo-states and a large maximum orbital angular momentum, $\ell_{\text{max}}$, of the included states are needed to accurately represent the electrons that are far from the target [34].

Using the effective potential we calculate radial wave functions for the active electron in the effective field of the $H_2^+$ ion by solving the Schrödinger equation. To this end, we apply an iterative Numerov approach. We take only those solutions with negative eigenvalues (energies) to construct the bound-state wave functions. To construct continuum pseudo-states, we subdivide the continuum of the electron into $N_c$ non-overlapping momentum intervals from $k_{\text{min}}$ to $k_{\text{max}}$. We then construct a wave packet $\psi_{n\ell m}^{\text{WP}}(\boldsymbol{r}) = \phi_{n\ell}^{\text{WP}}(r)Y_{\ell m}(\hat{\boldsymbol{r}})/r$ for each interval, which represents the active electron having momentum anywhere within the boundaries of that interval. The wave-packet radial wave function is constructed by numerically integrating the continuum wave over the momentum interval $[k_n, k_{n+1}]$ according to

$$\phi_{n\ell}^{\mathrm{WP}}(r) = A_n \int_{k_n}^{k_{n+1}} \mathrm{d}k \, \sqrt{k} \varphi_{k\ell}^{\mathrm{T}}(r). \tag{7}$$

The normalisation factor is given by

$$A_n = \sqrt{\frac{2}{k_{n+1}^2 - k_n^2}}. \tag{8}$$

The integral in Equation (7) is calculated numerically using a Gauss–Legendre quadrature and at each momentum-point an iterative Numerov approach is used to solve the target Schrödinger equation with energy $\varepsilon = k^2/2$ to obtain the continuum wave-function $\varphi_{k\ell}^{\mathrm{T}}(r)$. The energy of the $n$th continuum pseudo-state is given by

$$\varepsilon_n = \frac{k_n^2 + k_{n+1}^2}{4}, \tag{9}$$

which corresponds to the midpoint of the interval in energy space. The procedure is repeated for all $N_c$ intervals. The value of $k_{\mathrm{max}}$ is chosen to be sufficiently large so that the results of interest converge, and $k_{\mathrm{min}}$ is set very close to zero.

Combined, the set of negative- and positive-energy pseudo-states form an orthonormal basis that diagonalises the target Hamiltonian, i.e.,

$$\left\langle \psi_{\alpha'}^{\mathrm{T}} \middle| \psi_{\alpha}^{\mathrm{T}} \right\rangle = \delta_{\alpha'\alpha}, \quad \left\langle \psi_{\alpha'}^{\mathrm{T}} \middle| H_{\alpha} \middle| \psi_{\alpha}^{\mathrm{T}} \right\rangle = \delta_{\alpha'\alpha}\varepsilon_{\alpha}, \tag{10}$$

where the target states $\psi_{\alpha}^{\mathrm{T}}$ have energy $\varepsilon_{\alpha}$.

The projectile–atom states are constructed from eigenstates of the hydrogen atom and wave-packets made using the pure Coulomb wave function. Together, they also form an orthonormal basis that spans the negative- and positive-energy spectrum of the projectile atom,

$$\left\langle \psi_{\beta'}^{\mathrm{P}} \middle| \psi_{\beta}^{\mathrm{P}} \right\rangle = \delta_{\beta'\beta}, \quad \left\langle \psi_{\beta'}^{\mathrm{P}} \middle| H_{\beta} \middle| \psi_{\beta}^{\mathrm{P}} \right\rangle = \delta_{\beta'\beta}\varepsilon_{\beta}, \tag{11}$$

where $\varepsilon_{\beta}$ is given by the eigenvalues of the hydrogen atom for the bound-states and Equation (9) for the positive-energy pseudo-states.

The expansion of the total scattering wave function in Equation (6) is substituted into Equation (1). Using the semi-classical approximation, and, after some algebra, this results in the following set of first-order differential equations for the unknown expansion coefficients:

$$\begin{cases} i\dot{F}_{\alpha'} + i\sum\limits_{\beta=1}^{M} \dot{G}_{\beta}\tilde{K}_{\alpha'\beta} = \sum\limits_{\alpha=1}^{N} F_{\alpha}D_{\alpha'\alpha} + \sum\limits_{\beta=1}^{M} G_{\beta}\tilde{Q}_{\alpha'\beta}, \\ i\sum\limits_{\alpha=1}^{N} \dot{F}_{\alpha}K_{\beta'\alpha} + i\dot{G}_{\beta'} = \sum\limits_{\alpha=1}^{N} F_{\alpha}Q_{\beta'\alpha} + \sum\limits_{\beta=1}^{M} G_{\beta}\tilde{D}_{\beta'\beta}, \\ \alpha' = 1, 2, \ldots, N, \quad \beta' = 1, 2, \ldots, M. \end{cases} \tag{12}$$

$D_{\alpha'\alpha}$ are the direct-scattering matrix elements, $K_{\beta'\alpha}$ are the overlap integrals, and $Q_{\beta'\alpha}$ are the exchange matrix elements. Tildes indicate quantities in the projectile-centred coordinate system, and dots over $F_{\alpha}$ and $G_{\beta}$ denote time derivatives. The set of Equation (12) is solved for the time-dependent expansion coefficients $F_{\alpha}$ and $G_{\beta}$ subject to the boundary condition,

$$\begin{aligned} F_{\alpha}(-\infty, \boldsymbol{b}) &= \delta_{\alpha i}, \quad \alpha = 1, 2, \ldots, N, \\ G_{\beta}(-\infty, \boldsymbol{b}) &= 0, \quad \beta = 1, 2, \ldots, M, \end{aligned} \tag{13}$$

using the Runge–Kutta method. In the limit as $t \to +\infty$, the expansion coefficients, $F_\alpha(t, \boldsymbol{b})$ and $G_\beta(t, \boldsymbol{b})$, yield the scattering amplitudes for the final channel, specified by $\alpha$ and $\beta$, respectively.

Evaluation of the direct-scattering matrix elements is detailed in ref. [32]. The overlap integrals and rearrangement matrix elements are calculated in spheroidal coordinates according to the method described in ref. [26].

### 2.2. Scattering Amplitudes

The formal foundation for this study was laid in refs. [35,36]. According to these works, the post form of the scattering amplitude is given, in general, by

$$T_{fi}(\boldsymbol{q}_f, \boldsymbol{q}_i) = \left\langle \Phi_f^- \middle| \overleftarrow{H} - E \middle| \Psi_i^+ \right\rangle, \tag{14}$$

where $\boldsymbol{q}_f$ and $\boldsymbol{q}_i$ are the relative momenta of the projectile in the final and initial channels, respectively, and $\Phi_f^-$ is the asymptotic state in the final channel. The arrow over the Hamiltonian indicates the direction of its action. Depending on the outcome of scattering, $\Phi_f^-$ has a different form. In collisions without rearrangement (direct scattering), $\Phi_f^-$ is given by the product of a plane wave representing the relative motion of the projectile, $e^{i\boldsymbol{q}_\alpha \cdot \boldsymbol{\rho}}$, and a target wave function corresponding to final state $f$. If the active electron leaves the collision system with the projectile (electron capture) then $\Phi_f^-$ is made up of a plane wave representing the relative motion of the residual $H_2{}^+$ target ion, $e^{i\boldsymbol{q}_\beta \cdot \boldsymbol{\sigma}}$, and a wave function of the projectile atom corresponding to the final channel $f$.

In this work, we are interested in the ionisation amplitude. If scattering results in breakup, then the final state is given by the three-body asymptotic wave that represents the three unbound particles. In the WP-CCC approach to ionisation, we avoid the need to employ this result by, instead, inserting the identity operator, constructed from our square-integrable pseudo-states, into Equation (14); see ref. [25] for a detailed description of the method. As a result, the amplitude for ionisation into the continuum bin $f$ is given by the product of the overlap between the true continuum wave for electron momentum $\boldsymbol{\kappa}$ and the wave-packet pseudo-state bin that contains $\kappa$, and the amplitude for excitation into the corresponding pseudo-state. For a detailed description of the approach, see refs. [28,30,37]. Effectively, this replaces the non-$L^2$ continuum of the target (or projectile) with our square-integrable pseudo-states. This allows us to calculate the ionisation amplitude from the amplitudes for excitation into positive-energy pseudo-states. In this model, the ionisation amplitude contains two parts. The first represents direct ionisation (DI) and the second represents electron capture into the continuum (ECC) of the projectile. The DI and ECC amplitudes are given by

$$T_{fi}^{\mathrm{DI}}(\boldsymbol{\kappa}, \boldsymbol{q}_f, \boldsymbol{q}_i) = \frac{1}{(2\pi)^{3/2}} \sum_{\ell m} \left\langle \psi_{\boldsymbol{\kappa}}^{\mathrm{T}} \middle| \psi_f^{\mathrm{T}} \right\rangle T_{fi}^{\mathrm{DS}}(\boldsymbol{q}_f, \boldsymbol{q}_i), \tag{15}$$

and

$$T_{fi}^{\mathrm{ECC}}(\boldsymbol{\varkappa}, \boldsymbol{q}_f, \boldsymbol{q}_i) = \frac{1}{(2\pi)^{3/2}} \sum_{\ell m} \left\langle \psi_{\boldsymbol{\varkappa}}^{\mathrm{P}} \middle| \psi_f^{\mathrm{P}} \right\rangle T_{fi}^{\mathrm{EC}}(\boldsymbol{q}_f, \boldsymbol{q}_i), \tag{16}$$

where $T_{fi}^{\mathrm{DS}}$ and $T_{fi}^{\mathrm{EC}}$ are the direct-scattering (DS) and electron-capture (EC) amplitudes, respectively. Here, $\left\langle \psi_{\boldsymbol{\kappa}}^{\mathrm{T}} \middle| \psi_f^{\mathrm{T}} \right\rangle$ is the overlap of the true continuum wave, $\psi_{\boldsymbol{\kappa}}^{\mathrm{T}}$, in the target frame and the target pseudo-state, $\left\langle \psi_{\boldsymbol{\varkappa}}^{\mathrm{P}} \middle| \psi_f^{\mathrm{P}} \right\rangle$ is the overlap of the true continuum wave, $\psi_{\boldsymbol{\varkappa}}^{\mathrm{P}}$, in the projectile frame and the projectile pseudo-state. The summation on the RHS of Equations (15) and (16) accounts for the fact that the continuum pseudo-states are degenerate and, for each continuum bin, there exist multiple pseudo-states with differing orbital and magnetic quantum numbers, $\ell$ and $m$. Hence, the complete amplitude for DI, or ECC, into the final-channel bin $f$ that contains the momentum $\boldsymbol{\kappa}$, or $\boldsymbol{\varkappa}$, is given by the

sum of all degenerate pseudo-states constructed in that momentum interval. Furthermore, there is a subtlety in the difference in meaning of the amplitude on the RHS and LHS in these equations. The amplitude on the RHS corresponds to excitation into a positive-energy pseudo-state, i.e., a binary process. However, on the LHS the amplitude corresponds to ionisation, i.e., breakup. Specifically, $T_{fi}^{\mathrm{DS}}$ and $T_{fi}^{\mathrm{EC}}$ always represent a two-particle system, whereas $T_{fi}^{\mathrm{DI}}$ and $T_{fi}^{\mathrm{ECC}}$ correspond to a three-particle system with the electron being in the continuum. Hence, to obtain correctly normalised cross sections, the factor of $1/(2\pi)^{3/2}$ is introduced. This accounts for the density-of-states of the additional particle in the final channel.

The overlap of the wave-packet pseudo-state and true continuum wave is found by expanding the continuum wave in terms of partial waves, according to

$$\psi_{\boldsymbol{\kappa}}^{\mathrm{T}}(\boldsymbol{r}) = \frac{(2\pi)^{3/2}}{\kappa r}\sum_{\lambda\mu} i^{\lambda}\mathrm{e}^{-i\sigma_{\lambda}^{\mathrm{T}}}\varphi_{\kappa\lambda}^{\mathrm{T}*}(r)Y_{\lambda\mu}^{*}(\hat{\boldsymbol{r}})Y_{\lambda\mu}(\hat{\boldsymbol{\kappa}}), \tag{17}$$

where $\sigma_{\lambda}^{\mathrm{T}}$ is the phase shift and $\varphi_{\kappa\lambda}^{\mathrm{T}}(r)$ is the radial part of the continuum wave function of the target, both of which are obtained numerically by solving the corresponding Schrödinger equation for the positive-energy $\varepsilon = \kappa^2/2$. Substituting Equation (17) and the integral form of the wave-packet pseudo-states into the expression for the overlap integral, we obtain

$$\left\langle \psi_{\boldsymbol{\kappa}}^{\mathrm{T}} \middle| \psi_{f}^{\mathrm{T}} \right\rangle = \frac{(2\pi)^{3/2}A_n}{\sqrt{\kappa}}(-i)^{l}\mathrm{e}^{i\sigma_{l}^{\mathrm{T}}}Y_{lm}(\hat{\boldsymbol{\kappa}}). \tag{18}$$

Similarly, we write

$$\psi_{\boldsymbol{\varkappa}}^{\mathrm{P}}(\boldsymbol{r}) = \frac{(2\pi)^{3/2}}{\varkappa r}\sum_{\lambda\mu} i^{\lambda}\mathrm{e}^{-i\sigma_{\lambda}^{\mathrm{P}}}\varphi_{\varkappa\lambda}^{\mathrm{P}*}(r)Y_{\lambda\mu}^{*}(\hat{\boldsymbol{r}})Y_{\lambda\mu}(\hat{\boldsymbol{\varkappa}}), \tag{19}$$

where $\sigma_{\lambda}^{\mathrm{P}}$ is the Coulomb phase shift and $\varphi_{\varkappa\lambda}^{\mathrm{P}}(r)$ is the analytically known regular Coulomb wave function. With this, the overlap integral appearing in Equation (16) is given as

$$\left\langle \psi_{\boldsymbol{\varkappa}}^{\mathrm{P}} \middle| \psi_{f}^{\mathrm{P}} \right\rangle = \frac{(2\pi)^{3/2}A_n}{\sqrt{\varkappa}}(-i)^{l}\mathrm{e}^{i\sigma_{l}^{\mathrm{P}}}Y_{lm}(\hat{\boldsymbol{\varkappa}}). \tag{20}$$

The amplitudes in Equations (15) and (16) are written in momentum space. However, solving the coupled equations in Equation (12) leads to the expansion coefficients, $F_{\alpha}$ and $G_{\beta}$, that are written in impact–parameter space. Following the technique outlined in ref. [28] we used the Fourier–Bessel transform to calculate $T_{fi}^{\mathrm{DS}}$ from $F_{\alpha}$, according to

$$T_{fi}^{\mathrm{DS}}(\boldsymbol{q}_f, \boldsymbol{q}_i) = 2\pi i v \mathrm{e}^{im\phi_f}\int_0^{\infty} d\,bb[\tilde{F}_f(+\infty, b) - \delta_{fi}]J_m(q_{\perp}b), \tag{21}$$

and $T_{fi}^{\mathrm{EC}}$ from $G_{\beta}$ as

$$T_{fi}^{\mathrm{EC}}(\boldsymbol{q}_f, \boldsymbol{q}_i) = 2\pi i v \mathrm{e}^{im\phi_f}\int_0^{\infty} d\,bb\tilde{G}_f(+\infty, b)J_m(q_{\perp}b). \tag{22}$$

For direct ionisation, we have $f = \alpha$ and $\varepsilon_f > 0$ in Equation (21), and for electron capture into the continuum, $f = \beta$ and $\varepsilon_f > 0$ in Equation (22). In Equations (21) and (22) the perpendicular component of the momentum transfer $\boldsymbol{q} = \boldsymbol{q}_i - \boldsymbol{q}_f$ is $\boldsymbol{q}_{\perp}$, the azimuthal angle of the projectile momentum in the exit channel $\boldsymbol{q}_f$ is $\phi_f$, the change in magnetic quantum number from the initial to final channel is $m = m_f - m_i$, and $J_m$ is the Bessel function of the first kind of order $m$. $\tilde{F}_f(t, b) = \mathrm{e}^{im\phi_b}F_f(t, \boldsymbol{b})$ and $\tilde{G}_f(t, b) = \mathrm{e}^{im\phi_b}G_f(t, \boldsymbol{b})$ are the expansion coefficients that do not depend on the azimuthal angle of the impact parameter, i.e., the exponential factor containing the dependence on $\phi_b$ and $m$ has been factored out. That is to

say that Equations (21) and (22) are written in terms of expansion coefficients $F(t, \boldsymbol{b})$ and $G(t, \boldsymbol{b})$.

Numerical evaluation of the integrals in Equations (21) and (22) is difficult, due to the oscillatory nature of the integrand. We solve Equation (12) at 64 impact-parameter points from $b_{\min} = 0$ to $b_{\max} = 40$ a.u. In previous works [28,30], the calculated expansion coefficients were then interpolated onto a denser grid with 640 impact–parameter points before taking the integrals in Equations (21) and (22) to improve the efficiency of the calculations. However, in this work, we find that doubly differential cross sections are sensitive to $T_{fi}^{\mathrm{DS}}$ and $T_{fi}^{\mathrm{EC}}$ at momentum-transfer values as high as $q_{\perp} = 64$ a.u. This means the argument of the Bessel functions in Equations (21) and (22) is significantly larger, and, as a result, the integrand is required to be interpolated at a very large number of points. Therefore, we used the fast Hankel transform algorithm developed by Anderson [38]. This algorithm takes advantage of the fact that the Hankel transform can be expressed as a convolution and evaluated using a set of pre-calculated filter weights, removing the need to evaluate any Bessel functions during the calculation. We find that this method is capable of calculating $T_{fi}^{\mathrm{DS}}$ and $T_{fi}^{\mathrm{EC}}$ accurately for large values of $q_{\perp}$ and is approximately an order of magnitude faster than direct numerical integration.

### *2.3. Differential cross Sections*

After calculating the momentum–space transition amplitudes, using Equations (21) and (22), the DI and ECC amplitudes for ionisation are determined from Equations (15) and (16). The differential cross section can then be calculated. The fully differential cross section (FDCS) for ionisation is made up of two parts: direct ionisation, where the emitted electron is in the continuum of the target, and electron capture into the continuum, where the emitted electron is in the continuum of the projectile atom. In the WP-CCC approach to ionisation, the total breakup amplitude is given by the incoherent sum of these two parts [27]. However, the DI and ECC components are calculated in the target- and projectile-frames, respectively, as seen in Equations (15) and (16). Therefore, before combining them they must be brought into a common frame of reference. We choose the target-atom frame, since it corresponds to the laboratory frame where experimental measurements take place. Thus, only the ECC part needs to be transformed. This is done by substituting $\boldsymbol{\varkappa} \to \boldsymbol{\kappa} - \boldsymbol{v}$ and $\boldsymbol{q}_{\perp} \to (\boldsymbol{q} - \boldsymbol{\kappa})_{\perp}$ in Equations (16) and (22). However, the coefficients $G_{\beta}$ are calculated at discrete energies determined by the distribution of bins in the projectile-centred basis. Hence, they are interpolated over the momentum–space variables of the electron to the points corresponding to those in the target frame. This maps the ECC component to ejected-electron momenta that correspond to the predefined energies of the target atom continuum pseudo-states. Thus, the fully differential cross section for ionisation, resulting in emission of an electron with momentum within the $n$th continuum bin, is written as

$$\frac{\mathrm{d}^3\sigma_n}{\mathrm{d}E_{\mathrm{e}}\mathrm{d}\Omega_{\mathrm{e}}\mathrm{d}\Omega_f} = \frac{\mu_{\mathrm{T}}^2}{(2\pi)^2}\frac{q_f\kappa}{q_i}\left(\left|T_{fi}^{\mathrm{DI}}(\boldsymbol{\kappa}, \boldsymbol{q}_f, \boldsymbol{q}_i)\right|^2 + \left|T_{fi}^{\mathrm{ECC}}(\boldsymbol{\kappa} - \boldsymbol{v}, \boldsymbol{q}_f, \boldsymbol{q}_i)\right|^2\right), \tag{23}$$

where $E_{\mathrm{e}}$ is the energy of the ejected electron, $\Omega_{\mathrm{e}}$ is the solid angle into which the electron is ejected, and $\Omega_f$ is the solid angle the projectile is scattered into.

In Equation (23), the DI and ECC components are combined incoherently. Calculations of the DDCS for ionisation in p + H collisions [27] demonstrated the following: (i) the incoherent calculations are significantly less time-consuming than the coherent ones and (ii) the results obtained from the incoherent and coherent combinations of the DI and ECC components are practically the same if a sufficiently large number of states are used in the two-centre expansion (6). The latter indicates that the interference term appearing in the coherent combination is small. Furthermore, the TICS is given by the sum of the integrated cross sections for excitation into the positive-energy target pseudo-states and electron capture into the positive-energy projectile pseudo-states [32]. Therefore, the incoherent combination of the components in Equation (23) is consistent with the definition of the

TICS upon integration. This may indicate that in the close-coupling formalism the DI and ECC components should be added incoherently. A possible reason for this is that the DI and ECC components of the ionisation amplitude are calculated in the final channel, when the target and projectile are far apart [39]. Indeed, the DS and EC amplitudes entering Equations (15) and (16) are given by the Fourier transform of the impact–parameter space probability amplitudes (see Equations (21) and (22)). These probability amplitudes are found from the expansion coefficients in the limit as $t \to +\infty$, where there is no overlap between the target and projectile-centred basis states. Therefore, it is reasonable to assume that the interference term arising from a coherent combination of $T_{fi}^{\mathrm{DI}}$ and $T_{fi}^{\mathrm{ECC}}$ should approach zero.

The doubly differential cross section for ionisation, in terms of the electron kinematics, is given by integration of Equation (23) over the solid angle of the projectile

$$\frac{\mathrm{d}^2\sigma_n}{\mathrm{d}E_\mathrm{e}\mathrm{d}\Omega_\mathrm{e}} = \int \frac{\mathrm{d}^3\sigma_n}{\mathrm{d}E_\mathrm{e}\mathrm{d}\Omega_\mathrm{e}\mathrm{d}\Omega_f}\mathrm{d}\Omega_f. \tag{24}$$

This integration can be performed numerically using a Gauss–Legendre quadrature. The FDCS in Equation (24) is obtained by substituting Equations (18) and (20) into Equations (15) and (16), respectively, and, then, inserting the resulting expressions for $T_{fi}^{\mathrm{DI}}$ and $T_{fi}^{\mathrm{ECC}}$ into Equation (23). This leads to

$$\begin{aligned}\frac{\mathrm{d}^3\sigma_n}{\mathrm{d}E_\mathrm{e}\mathrm{d}\Omega_\mathrm{e}\mathrm{d}\Omega_f} =& A_n^2 \frac{\mu_\mathrm{T}^2}{(2\pi)^2}\frac{q_f\kappa}{q_i}\left(\left|\frac{1}{\sqrt{\kappa}}\sum_{\ell m}(-i)^l \mathrm{e}^{i\sigma_l^\mathrm{T}} Y_{lm}(\hat{\boldsymbol{\kappa}}) T_{fi}^{\mathrm{DS}}(\boldsymbol{q}_f,\boldsymbol{q}_i)\right|^2\right.\\ &\left.+\left|\frac{1}{\sqrt{\varkappa}}\sum_{\ell m}(-i)^l \mathrm{e}^{i\sigma_l^\mathrm{P}} Y_{lm}(\hat{\boldsymbol{\varkappa}}) T_{fi}^{\mathrm{EC}}(\boldsymbol{q}_f,\boldsymbol{q}_i)\right|^2\right),\end{aligned} \tag{25}$$

where we used $\varkappa$ to denote $|\boldsymbol{\kappa}-\boldsymbol{v}|$ and $\hat{\boldsymbol{\varkappa}}$ stands for $\widehat{\boldsymbol{\kappa}-\boldsymbol{v}}$. Alternatively, we can evaluate the integral in Equation (24) analytically. To do this we insert Equations (21) and (22) into Equation (25) and integrate over $\Omega_f$ using the rectilinear approximation

$$\int \mathrm{d}\Omega_f = \frac{1}{q_i q_f}\int_0^{2\pi}\mathrm{d}\phi_f \int_0^\infty \mathrm{d}q_\perp q_\perp. \tag{26}$$

This allows us to take the integral over the azimuthal angle according to

$$\int_0^{2\pi}\mathrm{d}\phi_f \mathrm{e}^{i(m'-m)\phi_f} = 2\pi\delta(m'-m). \tag{27}$$

Then, we use the orthogonallity of Bessel functions,

$$\int_0^\infty \mathrm{d}q_\perp q_\perp J_m(q_\perp b) J_m(q_\perp b') = \frac{\delta(b-b')}{b}, \tag{28}$$

to take the integral over the perpendicular component of the momentum transfer. The resulting expression for the DDCS in Equation (24) reads as

$$\begin{aligned}\frac{\mathrm{d}^2\sigma_n}{\mathrm{d}E_\mathrm{e}\mathrm{d}\Omega_\mathrm{e}} =& 2\pi A_n^2\left(\sum_{\ell=0}^{\ell_{\max}}\sum_{\ell'=0}^{\ell'_{\max}}\sum_{m=-\ell}^{\ell} Y_{\ell m}^*(\hat{\boldsymbol{\kappa}}) Y_{\ell' m}(\hat{\boldsymbol{\kappa}})(-i)^{\ell'-\ell}\mathrm{e}^{i(\sigma_{\ell'}^\mathrm{T}-\sigma_\ell^\mathrm{T})}\right.\\ &\times\int \mathrm{d}b\, b \tilde{F}_{nlm}^*(\infty,b)\tilde{F}_{n\ell' m}(\infty,b) + \sqrt{\frac{\kappa}{\varkappa}}\sum_{\ell=0}^{\ell_{\max}}\sum_{\ell'=0}^{\ell'_{\max}}\sum_{m=-\ell}^{\ell}\\ &\left.\times Y_{\ell m}^*(\hat{\boldsymbol{\varkappa}}) Y_{\ell' m}(\hat{\boldsymbol{\varkappa}})(-i)^{\ell'-\ell}\mathrm{e}^{i(\sigma_{\ell'}^\mathrm{P}-\sigma_\ell^\mathrm{P})}\int \mathrm{d}b\, b\, \tilde{G}_{nlm}^*(\infty,b)\tilde{G}_{n\ell' m}(\infty,b)\right).\end{aligned} \tag{29}$$

Equation (29) is the DDCS for ionisation resulting in electron emission along the surface of a cone at an angle of $\theta_e$ to the $z$-axis with a momentum between the boundaries of the $n$th continuum bin.

## 3. Results

In this section, we present the results of our calculations for the doubly differential cross section for ionisation in $p + H_2$ collisions. Each figure below shows the DDCS at a fixed impact energy and the individual panels correspond to different emission angles. At the top of each panel we also show the speed of the ejected electron $v_e$, in terms of the projectile speed. In the forward direction the ECC component peaks when $v_e/v = 1$. The smallest emission angle considered here is 10°. Nevertheless, the presence of the ECC peak is still observed, though to a lesser extent, even for 10° emission. We find that a basis containing $10 - \ell$ bound states for each included orbital quantum number $\ell$ up to $\ell_{max} = 3$ was sufficient to obtain converged results at all impact energies considered here. The continuum was discretised with 25 bins and the electron–momentum cutoff varied from $\kappa_{max} = 6.0$ a.u. to $\kappa_{max} = 10.0$ a.u., depending on the impact energy. The $z$-grid was extended from $-200$ to $+200$ a.u. The results obtained from Equation (29) are labelled as WP-CCC.

There are many combinations of ejection angle and ejection energy at different incident energies for which experimental data exist. Here, we present the results for a wide range of ejection energies and ejection angles for impact energies from 48 to 200 keV, and compared these with the available experimental data. Where possible, we also compared to previous calculations existing in the literature. In most of the panels we also show the DI and ECC components of the cross section. We omitted these lines in the panels that contain other calculations to prevent crowding of the figures.

Error bars for the experimental data are only given by Kuyatt and Jorgensen [14], and only for a few of their data points. However, this is the oldest data available and more recent works call into question the accuracy of their low-energy points [11], suggesting a potentially larger uncertainty in their results than estimated in the original work. There are no error bars available for the other experimental data shown in the figures presented below, but a discussion of the estimated uncertainties is given in the original sources. Specifically, the data of Rudd et al. [16] have an estimated uncertainty of 30%. The experimental data by Gealy et al. [11] has an uncertainty of 21% at 1.5 eV, decreasing to 18% at ejection energies greater than 10 eV. However, at the highest ejection energies recorded the authors estimated at least a 50% uncertainty, due to the low count rates recorded in the experiment.

In Figures 1 and 2 we present our results of the DDCS for ionisation as a function of the energy of the ejected electron at various emission angles for projectile energies of 48 and 67 keV. Here, the projectile speeds were $v = 1.386$ and 1.638 a.u., respectively. The only available data for the DDCS of ionisation at these energies were the measurements by Gealy et al. [11]. To our best knowledge there are no other calculations at these collision energies. For ejection angles of 110° and smaller we observed excellent agreement between our results and the experimental data. At 130 and 150° our DDCS agreed well with experiments for low-energy electrons but for high-energy electrons the WP-CCC approach overestimated the experimentally measured cross section at backward emission angles. There could be two possible explanations for this. First, this is the region in which the DDCS is several orders of magnitude smaller than for low-energy electrons and, therefore, the experimental measurements have the greatest uncertainty due to low counting rates. Second, ionisation resulting in emission in the backward direction is dominated by the DI mechanism. The DI component of the ionisation cross section is given by the product of the amplitude for excitation into a positive-energy pseudo-state and the overlap between the true continuum wave and corresponding wave-packet pseudo-state. The pseudo-states and continuum wave are both found by numerically solving the Schrödinger equation of the model target potential. At asymptotically large distances this potential tends towards a Coulomb attraction with charge $+1$ a.u. However, in reality the electron would be on the opposite side of the residual target ion from the projectile proton, resulting in an effective

Coulomb interaction at asymptotically large distances with charge +2 a.u. Hence, in our approach to calculating DI the emitted electron does not account for the additional attraction, due to the projectile proton. Therefore, the current approach may somewhat overestimate the probability of emission in the backward direction.

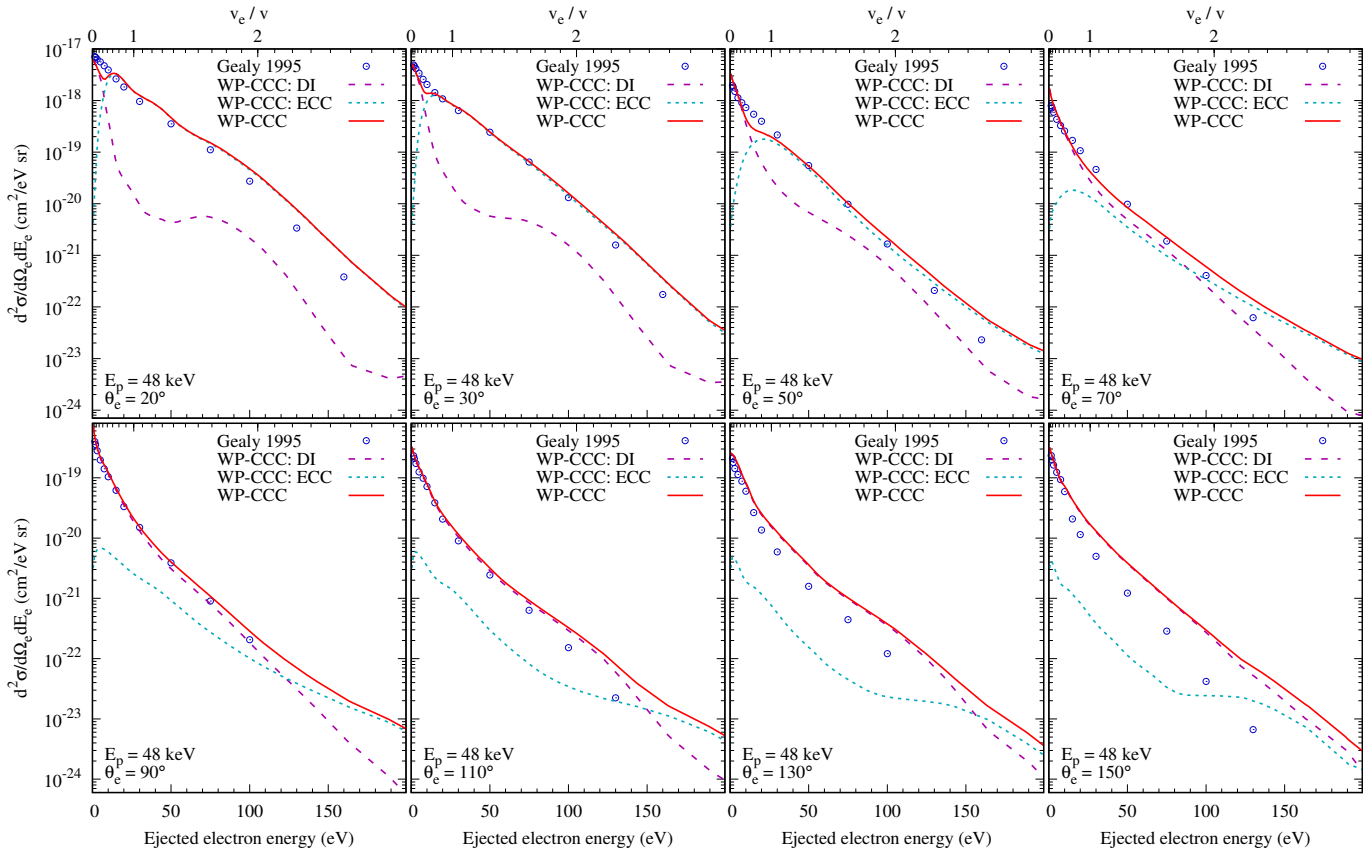


**Figure 1.** Doubly differential cross section of ionisation for 48 keV collisions with $H_2$ as a function of the ejected electron energy at various emission angles. Experimental data are by Gealy et al. [11]. Theoretical results: the WP-CCC approach. The present DI and ECC components are also shown.

Figure 3 shows the DDCS for ionisation at 75 keV for ejection angles from 10 to 160°. For the smallest emission angle we found that the ECC component of the DDCS peaked when the speed of the ejected electron was slightly less than that of the projectile, meaning that the likelihood of the electron staying slightly behind the outgoing projectile was higher. The projectile speed was $v = 1.733$ a.u. at this impact energy. The ECC peak was strongest for emission at 0°. Our calculations suggested it had an influence on the cross section for emission, even at 10°. At 60°, the DI and ECC components were comparable for most of the considered electron energies. Then, for emission into angles of 90° and greater, the DI became the dominant mechanism contributing to the total DDCS for ionisation. Only for very high electron energies did the ECC component have a significant effect on the overall results at 120, 140 and 160°. For emission into the backwards direction the DDCS was entirely dominated by DI, as expected.

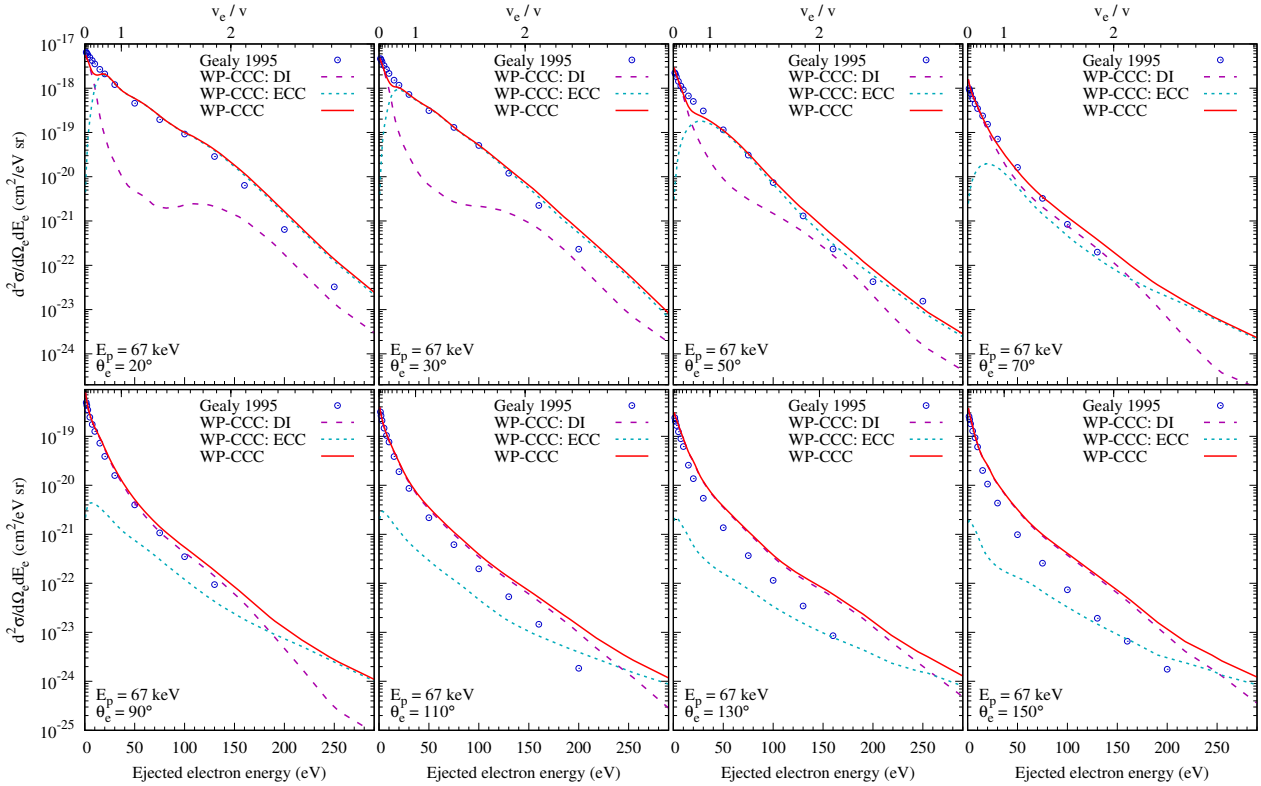


**Figure 2.** Same as Figure 1 but for 67 keV.

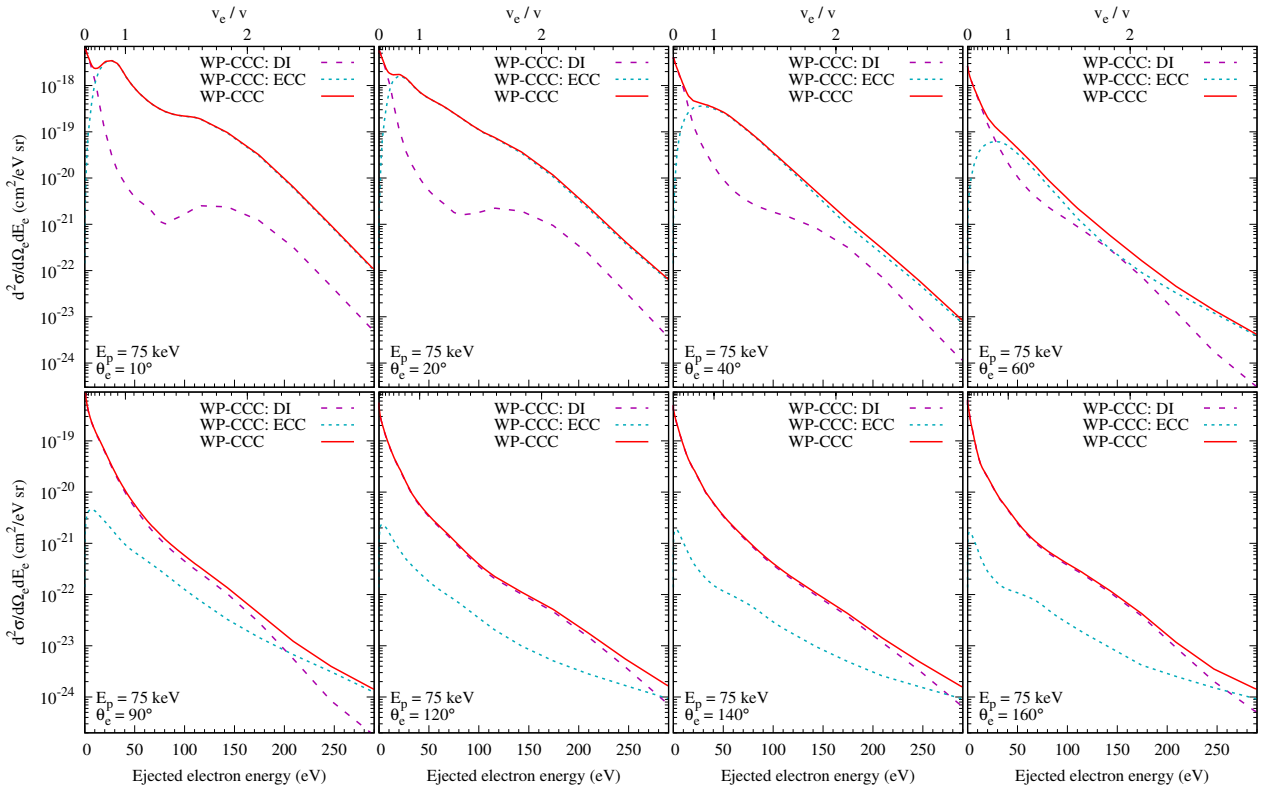


**Figure 3.** Doubly differential cross section of ionisation for 75 keV collisions with $H_2$ as a function of the ejected electron energy at various emission angles. Theoretical results: the WP-CCC approach. The present DI and ECC components are also shown.

In Figure 4 we present our results for the DDCS for ionisation at 95 keV for ejection angles from 20 to 150°. The projectile speed at this energy was $v = 1.950$ a.u. Our results were compared with the experimental data of Gealy et al. [11]. To our best knowledge there are no other experimental measurements or calculations at this collision energy. We observed very good agreement between the WP-CCC calculations and the experimental data. At the smallest considered ejection angle of 20°, the interplay between the DI and ECC contributions near the matching speed resulted in an overall smoother cross section that followed the experimental data more closely than observed at lower projectile energies. At this incident energy we also saw improved agreement between our results and the experimental data for high-energy electrons emitted at 130 and 150° degrees, compared to 48 and 67 keV.

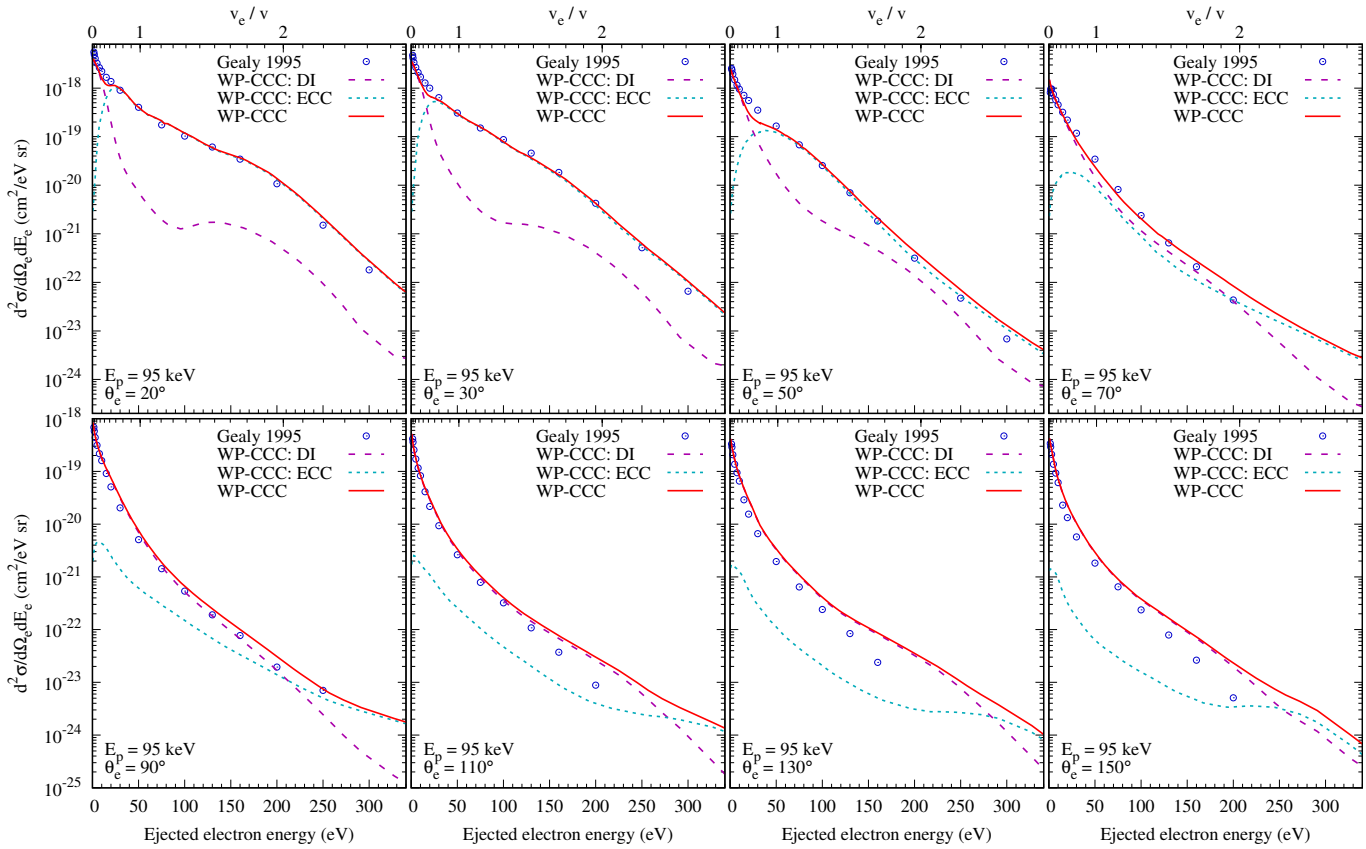


**Figure 4.** Same as Figure 1 but for 95 keV.

Figure 5 shows the DDCS for ionisation at 100 keV. Here, we compared our results with the experimental data of Rudd and Jorgensen [15] and Kuyatt and Jorgensen [14]. Rudd and Jorgensen [15] also performed the FBA calculations. The FBA results significantly underestimated the cross section at an emission angle of 10°, whereas the WP-CCC calculations showed excellent agreement with the experimental data across the entire measured energy range from threshold to 300 eV. We also saw a clear shoulder, due to the ECC peak for emission at 10°, in both the experimental data and our calculations. At this impact energy, the matching speed was $v = 2.000$ a.u. At 23° the WP-CCC results agreed well with the experimental data of Kuyatt and Jorgensen [14], except for small energies of the emitted electrons. However, these experimental data were unreliable in that region, due to inefficiencies in the apparatus at detecting low-energy electrons [11]. In this energy region the DDCS was dominated by the DI mechanism. At energies above 30 eV, ECC was the most significant contributor to the ionisation cross section. At 30°, the FBA calculations continued to underestimate the experimental data, although less significantly, whereas the WP-CCC calculations followed the experiment very closely at all ejection energies. For

emission into an angle of 45°, we found good agreement with the experimental results of Kuyatt and Jorgensen [14], except for the narrow region near the ejection energy of 30 eV, where the DI and ECC components contributed equally to the ionisation cross section. Here, our calculation underestimated the experiment. At an emission angle of 50°, we also observed a similar difference between our result and the experimental data of Rudd and Jorgensen [15]. However, the difference was smaller than at 45°. For ionisation resulting in electron emission at 70°, the WP-CCC results agreed well with the experimental data, although as the ejection energy increased our results began to underestimate the measured cross section. The FBA calculations by Rudd and Jorgensen [15] showed similar behaviour, except beyond 100 eV, they fell off more steeply, deviating from the experiment and the WP-CCC calculations. The FBA results showed similar behaviour also at 90°, whereas the WP-CCC results displayed excellent agreement with the experiment emission energies. Lastly, at 160° emission the FBA overestimated the experimental cross section near the ionisation threshold and then fell off too steeply with increasing energy. Our calculations agreed well with the data of Rudd and Jorgensen [15] for low-energy electron emission, slightly underestimating the experimental data above 50 eV.

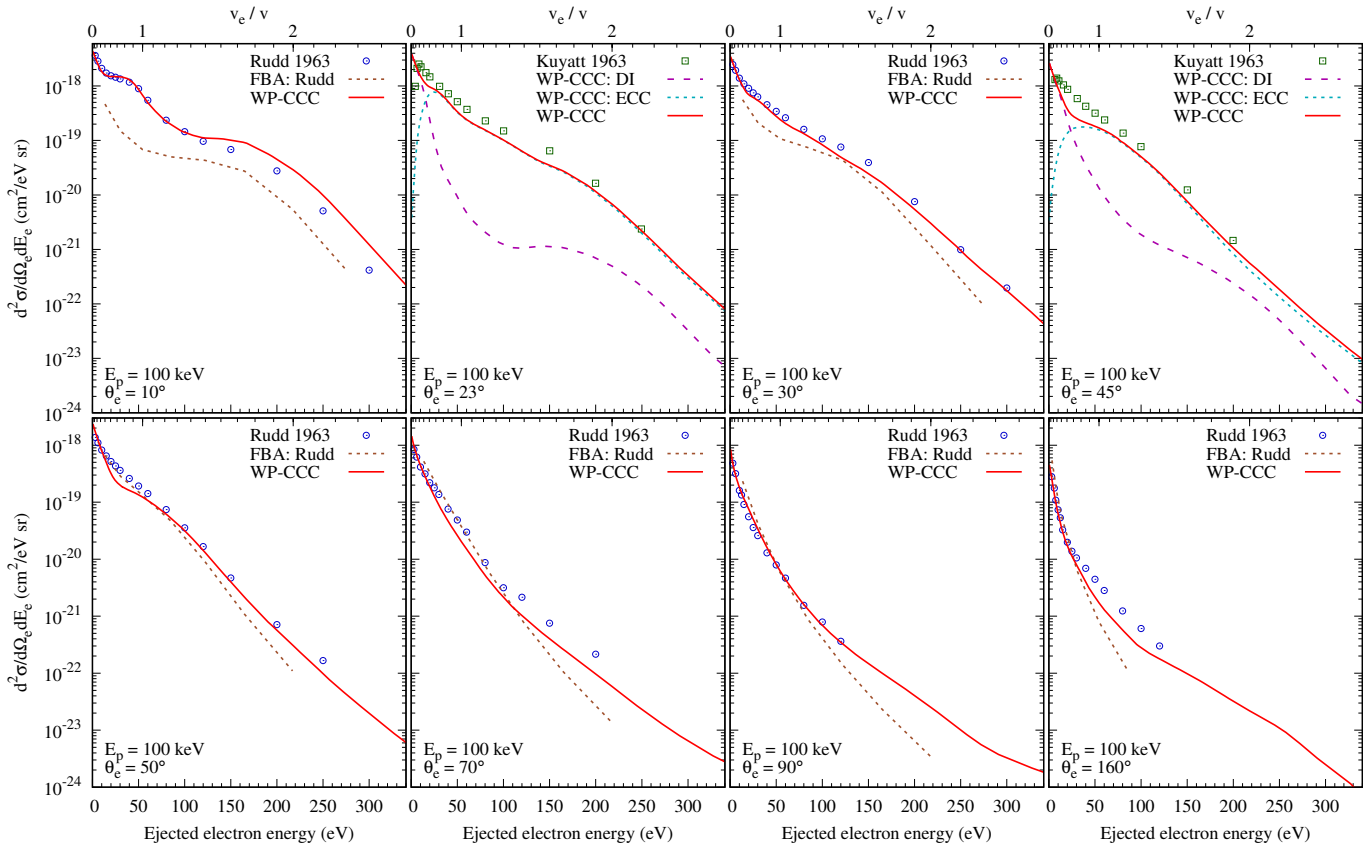


**Figure 5.** Doubly differential cross section of ionisation for 100 keV proton collisions with $H_2$ as a function of the ejected electron energy at various emission angles. Experimental data are by Kuyatt and Jorgensen [14], and Rudd and Jorgensen [15]. Theoretical results: the WP-CCC approach and the first-order Born approximation by Rudd and Jorgensen [15]. The present DI and ECC components are also shown.

Figure 6 shows the DDCS at an incident energy of 114 keV, along with the experimental data of Gealy et al. [11] and the FBA and CDW-EIS-MO calculations by Galassi et al. [23]. The projectile speed was $v = 2.136$ a.u. At an emission angle of 20°, the WP-CCC calculations agreed very well with the experimental data below 250 eV emission energy. Above 250 eV, however, our results slightly overestimated the experiment. The same was observed at 30 and 50°. The FBA calculations of Galassi et al. [23] suggested a shoulder at 150 eV

for 30° emission, which was not present in the other calculations or experimental data. At 30 and 50°, the CDW-EIS-MO results agreed well with the experiment. At 70° and above, the WP-CCC results agreed well with the experimental data for smaller ejection energies, then tended to overestimate the data as the emission angle and energy increased. At emission angles of 90 and 150°, the FBA results overestimated the cross section for low-energy electron emission, but agreed well with the experimental data at high ejection energies. The CDW–EIS–MO calculations showed the opposite behaviour, agreeing well with the experiment at small ejection energies, but underestimating it at larger emission energies. We concluded that the WP–CCC method reproduced the experimental cross section more consistently than the FBA and CDW–EIS–MO methods.

In Figure 7 we present our results for a collision energy of 200 keV in comparison with the experimental data of Rudd et al. [16]. For emission into 10°, the experiment showed a clear shoulder near the matching speed of $v = 2.829$ a.u., which was perfectly reproduced by the WP-CCC results. We found good agreement between the WP-CCC results and experimental data across all ejection angles and energies for which experimental data was available. At the emission angles of 10, 30 and 70°, our calculations slightly deviated from the experimental data when moderate-energy electrons were emitted. At this impact energy, we saw the binary-encounter peak clearly resolved at small emission angles. In particular, at 10°, our calculations showed a wide, but pronounced, peak at 350 eV, reproducing the shape of the measured cross section. There was no experiment at 130°. Here, the WP-CCC results are given for completeness.

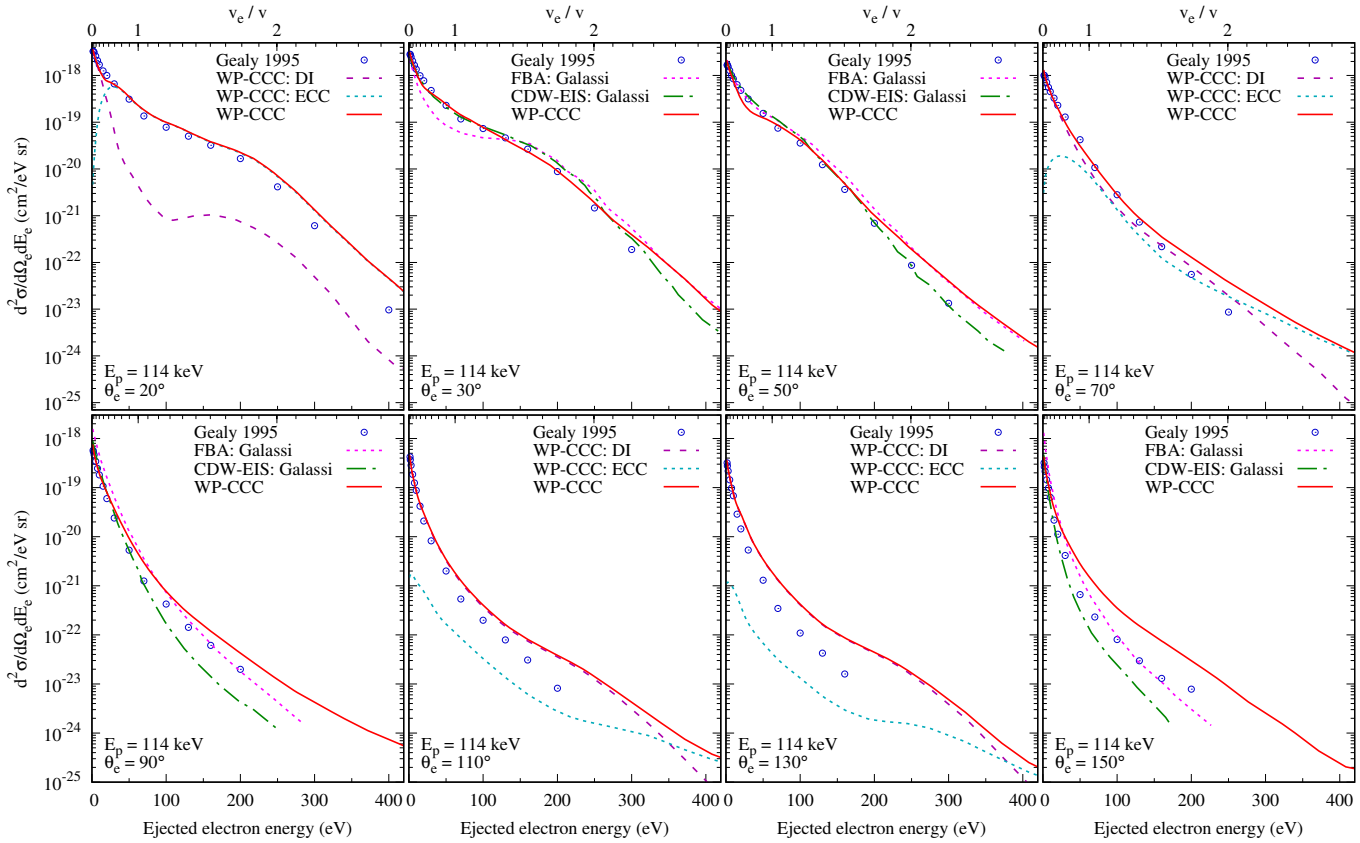


**Figure 6.** Doubly differential cross section of ionisation for 114 keV proton collisions with $H_2$ as a function of the ejected electron energy at various emission angles. Experimental data are by Gealy et al. [11]. Theoretical results: the WP-CCC approach and the first-order Born approximation and continuum distorted wave–eikonal initial state molecular-orbital method by Galassi et al. [23]. The present DI and ECC components are also shown.

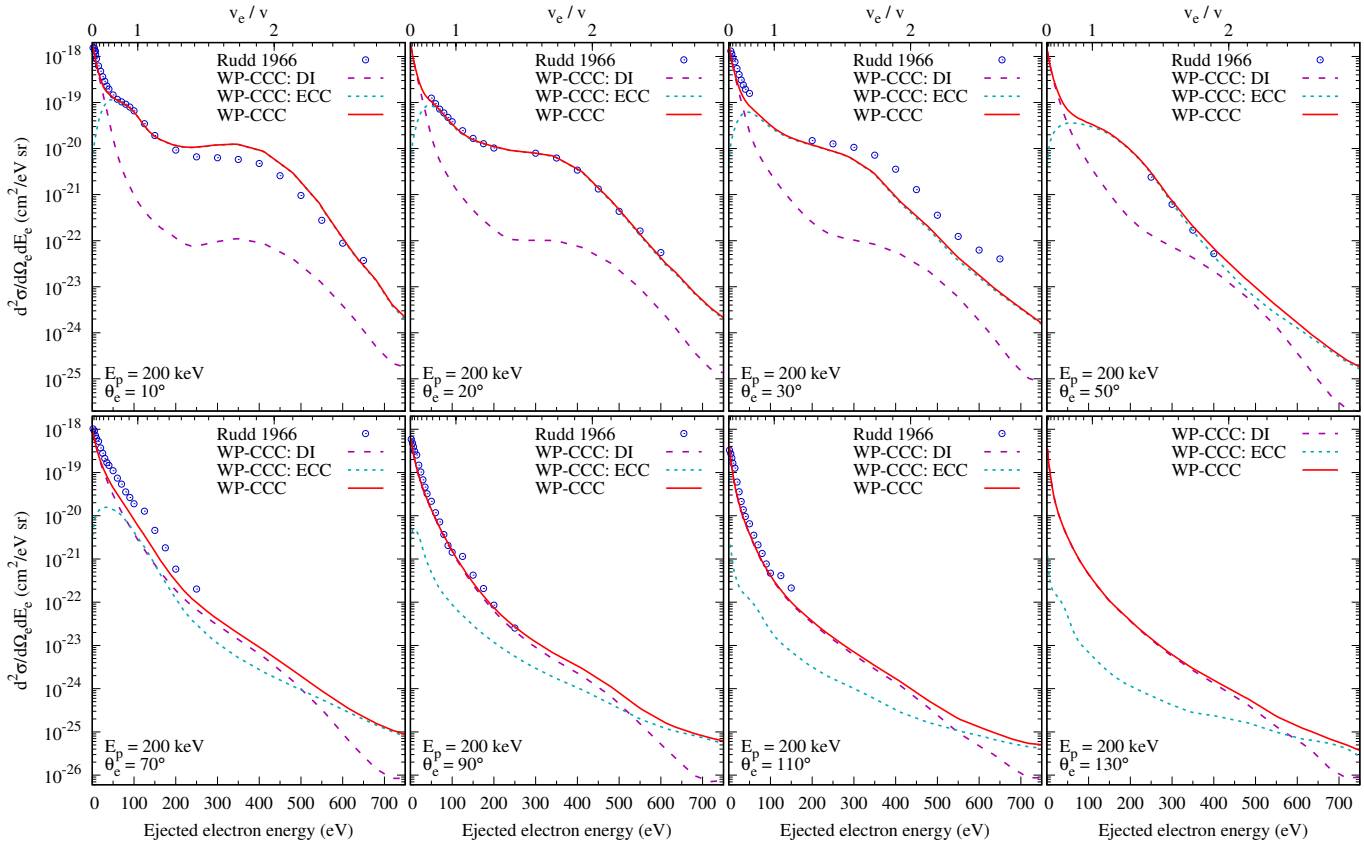


**Figure 7.** Doubly differential cross section of ionisation for 200 keV proton collisions with $H_2$ as a function of the ejected electron energy at various emission angles. Experimental data are by Rudd et al. [16]. Theoretical results: the WP-CCC approach. The present DI and ECC components are also shown.

At all impact energies considered we also calculated the DDCS via numerical integration over the fully differential cross section; see Equations (23) and (24). In all cases, the results were very similar to those found from analytical integration. At all impact energies considered, there was a slight difference at large ejection energies, where the "analytic" WP-CCC result was, generally, marginally larger than the "numerical" WP-CCC calculations, especially for ejection into angles greater than 70°. However, this happened only at the largest emission energies, where the corresponding DDCS was extremely small. Thus, overall excellent agreement between the "numerical" and "analytical" WP-CCC results provided a reassuring self-consistency check for our calculations. Additionally, the accuracy of the numerical integration was checked by increasing the density of integration points until convergence was obtained in the result. Thus, we could conclude that the small differences observed between the numerical and analytical WP-CCC calculations were the result of the interpolation of the ECC amplitudes when transforming them into the common laboratory frame. To obtain the numerical WP-CCC results, we interpolated the expansion coefficients $G_f(\infty, b)$, as discussed in Section 2.3. However, to obtain the ECC component of the cross section for the analytical WP-CCC results, we interpolated the integral appearing in the second term of Equation (29). This quantity, known as the density matrix, is also smooth but has a different structure. Hence, we concluded that the difference between our numerical and analytical WP-CCC results provided an estimate of the uncertainty associated with the interpolation procedure used to bring the ECC amplitudes into a common frame with the DI part. The difference was insignificant.

The results given in Figures 1–7 represent the doubly differential ionisation cross section as a function of two variables. Integrating them over either the emission angle or energy of the ejected electron resulted in the singly differential cross section for ionisation

as a function of the remaining variable. We performed this integration numerically and compared the results to our earlier calculations of the SDCS for ionisation presented in ref. [30]. Both types of the SDCS obtained from the DDCS presented here agreed perfectly with the previously published results. Furthermore, we integrated each of these two SDCS and found that the result was in very good agreement with the TICS calculated directly from the expansion coefficients [32].

Let us now outline the overall picture. In general, we found excellent agreement between the WP-CCC results and the experimental data of Rudd et al. [16], but our calculated cross section was slightly smaller than the experimental points from Rudd [40]. Agreement between our calculations and the data of Gealy et al. [11] was best at small ejection angles and larger impact energies. We observed the largest difference at high ejection energies for ejection in the backward direction. We saw a small dip in the calculated cross section at low ejection energies, where the DI and ECC components contributed equally, that was not reflected in the experimental data. We compared our results to the FBA and CDW–EIS–MO calculations of Galassi et al. [23] at ejection angles of 30, 50, 90, and 150°, available for an impact energy of 114 keV. Agreement between the FBA results and experimental data of Gealy et al. [11] varied considerably between different ejection angles. At 30°, the FBA calculations underestimated the experimental data around 60 eV, then overestimated it starting from 150 eV. At larger ejection angles the overall trend agreed better with the experimental points, except at small ejection energies, where the FBA results significantly overestimated the cross section at backward ejection angles. The CDW–EIS–MO calculations are the most sophisticated calculations currently available in the literature. They agreed slightly better with the experimental data at 50° than the WP-CCC results, but, at larger ejection angles, they began to underestimate the experimental cross section as the ejection energy increased. Thus, we concluded that, overall, the present WP-CCC method could accurately model the underlying physics and provide reliable DDCS for ionisation in the $p + H_2$ collisions.

Across all impact energies considered we found that, for small ejection angles, DI and ECC dominated the DDCS for small and large emission energies, respectively. The DI and ECC components were comparable to one another at an emission angle of about 70° for all projectile energies. For ejection at 90° and above, DI contributed the most to the DDCS. ECC was significant only for very large electron energies when the emission angle was greater than 90°. For emission into angles greater than 110°, our results overestimated the experimental data for high-energy electrons. Further investigation, with an improved target description, is required to understand this discrepancy between theory and experiment.

## 4. Conclusions

We applied the wave-packet convergent close-coupling approach to proton collisions with molecular hydrogen to calculate the ionisation cross section differential in both the angle and energy of the ejected electrons. A wide range of experimental results exist, spanning from the initial measurements of Kuyatt and Jorgensen [14] to the latest data of Gealy et al. [11]. However, theorists have struggled to accurately reproduce these experiments. All currently available theoretical results are obtained using perturbative approaches that are applicable only at sufficiently high projectile energies. The fundamental assumptions that these methods are based on become questionable at the incident energies considered in this work, where the orbital speed of the target electrons is comparable to, or somewhat greater than, the projectile speed. The present WP-CCC method is the first non-perturbative approach to differential ionisation that is applicable at all considered incident energies. Furthermore, it is the only method applied to this collision problem that accounts for the strong coupling between reaction channels, including capture into the continuum. Our results demonstrate excellent agreement with all available experimental data at projectile energies from 48 to 200 keV and electron emission angles less than 130°. We observed a consistent overestimation of the experimental data for emission into backward angles greater than 130°. It is suggested that this may be due to the large uncertainty in

the experimental data in this region. In part, this could also be due to the approach to calculating the total breakup amplitude used herein that assumes a weaker effective charge experienced by the emitted electron at asymptotically large distances from the origin than it actually might be in this particular kinematic regime.

Our results agree particularly well with the most recent experiment by Gealy et al. [11] and the high projectile energy data by Rudd et al. [16]. At the highest impact energies considered the WP-CCC method reproduces both the main peak in the DDCS near the ionisation threshold and the binary-encounter peak. Furthermore, we explicitly calculated direct ionisation and electron capture into the continuum contributions to the DDCS. This allowed us to analyse the roles these mechanisms play in emission of electrons in a wide range of kinematic regimes.

This work paves the way for applying the WP-CCC approach to calculations of the other types of DDCS for ionisation, such as that where the differential is in both the scattering angle of the projectile and the ejected electron energy [41,42]. Next, we plan to extend our calculations to ionisation resulting in emission in the forward direction, where ECC dominates the DDCS. Calculating the DDCS for ionisation in the forward direction has proven a challenging problem. Theoretical investigations are limited to the narrow region where the emitted electron velocity matches the projectile one. So far, there is no theory that properly describes the entire energy range of electrons ejected in the forward direction, including the low-energy and velocity-matching regions. The WP-CCC approach may be able to provide new insight into this problem.

We also plan to apply the two-centre WP-CCC method to calculate the doubly and fully differential cross sections for ionisation of both $H_2$ and He by proton impact. We recently calculated doubly differential cross sections for ionisation in proton–helium collisions and obtained excellent agreement with the available experimental data [43,44]. Currently, there is no theory that can describe the experimental data for the fully differential cross section at 75 keV, recently measured consistently by Schulz et al. [45] and Dhital et al. [9] in all kinematic regimes. Existing theoretical methods deviate from one another significantly and cannot reproduce the experiment well. The single-centre version of the WP-CCC has already been applied to the fully differential cross sections for ionisation in proton–helium collisions [46,47] at sufficiently high impact energies, where the electron-capture channels are believed to be negligible. The results agreed very well with the recent high-resolution experiment by Gassert et al. [48]. However, the approach predicted a slight, but unexpected, shift in the position of the binary peak compared to the experimental data. Furthermore, recent measurements of the fully differential cross section for ionisation in $p + H_2$ collisions in various geometries also demonstrate significant differences with currently available distorted-wave theories [9]. We intend to apply the two-centre WP-CCC method to calculate the fully differential cross sections in proton collisions with helium and molecular hydrogen to determine if higher-order effects, resulting from the presence of the second centre, are able to explain the aforementioned discrepancies.

**Author Contributions:** Methodology, C.T.P., K.H.S. and A.S.K.; Software, C.T.P. and K.H.S.; Investigation, C.T.P. and A.S.K.; Conceptualization & supervision, A.S.K.; Writing—original draft, C.T.P. and A.S.K.; Writing—review & editing, K.H.S. All authors have read and agreed to the published version of the manuscript.

**Funding:** This research received no external funding.

**Institutional Review Board Statement:** Not applicable.

**Informed Consent Statement:** Not applicable.

**Data Availability Statement:** All the data reported in this work are available on request from the authors.

**Acknowledgments:** This work was supported by the Australian Research Council. We also acknowledge the resources and services of the Pawsey Supercomputer Centre and the National Computing Infrastructure. C.T.P. acknowledges support through an Australian Government Research Training Program Scholarship. K.H.S. acknowledges the contribution of an Australian Government Research Training Program Scholarship, and the support of the Forrest Research Foundation. A.S.K. thanks Marko Horbatsch and Reinhard Dörner for stimulating discussions.

**Conflicts of Interest:** The authors declare no conflict of interest.

## References

1. Abril, I.; Garcia-Molina, R.; de Vera, P.; Kyriakou, I.; Emfietzoglou, D. Inelastic Collisions of Energetic Protons in Biological Media. *Adv. Quantum Chem.* **2013**, *65*, 129.
2. Marchuk, O. The status of atomic models for beam emission spectroscopy in fusion plasmas. *Phys. Scr.* **2014**, *89*, 114010. [CrossRef]
3. Belkić, D.; Bray, I.; Kadyrov, A. (Eds.) *State-of-the-Art Reviews on Energetic Ion-Atom and Ion-Molecule Collisions*; World Scientific: Singapore, 2019
4. Schulz, M. (Ed.) *Ion-Atom Collisions: The Few-Body Problem in Dynamic Systems*; De Gruyter: Berlin, Germany, 2019.
5. Abdurakhmanov, I.B.; Bray, I.; Fursa, D.V.; Kadyrov, A.S.; Stelbovics, A.T. Fully differential cross section for single ionization in energetic $C^{6+}-$He collisions. *Phys. Rev. A* **2012**, *86*, 034701. [CrossRef]
6. Schulz, M.; Moshammer, R.; Fischer, D.; Kollmus, H.; Madison, D.H.; Jones, S.; Ullrich, J. Three-dimensional imaging of atomic four-body processes. *Nature* **2003**, *422*, 48. [CrossRef] [PubMed]
7. Hasan, A.; Arthanayaka, T.; Lamichhane, B.; Sharma, S.; Gurung, S.; Remolina, J.; Akula, S.; Madison, D.H.; Ciappina, M.F.; Rivarola, R.D.; et al. Fully differential study of ionization in p + $H_2$ collisions near electron—Projectile velocity matching. *J. Phys. B* **2016**, *49*, 04LT01. [CrossRef]
8. Igarashi, A.; Gulyás, L. Differential cross sections for ionizations of H and $H_2$ by 75 keV proton impact. *J. Phys. B* **2018**, *51*, 035201. [CrossRef]
9. Dhital, M.; Bastola, S.; Silvus, A.; Davis, J.; Lamichhane, B.; Ali, E.; Ciappina, M.; Lomsadze, R.; Hasan, A.; Madison, D.H.; et al. Ejected-electron-energy and angular dependence of fully differential ionization cross sections in medium-velocity proton collisions with He and $H_2$. *Phys. Rev. A* **2020**, *102*, 032818. [CrossRef]
10. Belkić, D. Review of theories on ionization in fast ion-atom collisions with prospects for applications to hadron therapy. *J. Math. Chem.* **2010**, *47*, 1366. [CrossRef]
11. Gealy, M.W.; Kerby, G.W.; Hsu, Y.-Y.; Rudd, M.E. Energy and angular distributions of electrons from ion impact on atomic and molecular hydrogen. I. 20–114-keV $H^+$ + $H_2$. *Phys. Rev. A* **1995**, *51*, 2247. [CrossRef]
12. Rudd, M.; Kim, Y.; Madison, D.; Gallagher, J. Electron production in proton collisions: Total cross sections. *Rev. Mod. Phys.* **1985**, *57*, 965. [CrossRef]
13. Rudd, M.E.; Kim, Y.K.; Madison, D.H.; Gay, T.J. Electron production in proton collisions with atoms and molecules: Energy distributions. *Rev. Mod. Phys.* **1992**, *64*, 441. [CrossRef]
14. Kuyatt, C.E.; Jorgensen, T. Energy and Angular Dependence of the Differential Cross Section for Production of Electrons by 50–100 keV Protons in Hydrogen Gas. *Phys. Rev.* **1963**, *130*, 1444. [CrossRef]
15. Rudd, M.E.; Jorgensen, T. Energy and Angular Distribution of Electrons Ejected from Hydrogen and Helium Gas by Protons. *Phys. Rev.* **1963**, *131*, 666. [CrossRef]
16. Rudd, M.E.; Sautter, C.A.; Bailey, C.L. Energy and Angular Distributions of Electrons Ejected from Hydrogen and Helium by 100- to 300-keV Protons. *Phys. Rev.* **1966**, *151*, 20. [CrossRef]
17. Toburen, L.H.; Wilson, W.E. Distributions in Energy and Angle of Electrons Ejected from Molecular Hydrogen by 0.3-1.5-MeV Protons. *Phys. Rev. A* **1972**, *5*, 247. [CrossRef]
18. Gibson, D.K.; Reid, I.D. *Double Differential Cross Sections for Electrons Ejected from $H_2$, $O_2$, $N_2$, $CO_2$, $CH_4$, $H_2O$ and Ar by 50 keV Protons*; Report AAEC/E659; Australian Atomic Energy Commission: Lucas Heights, NSW, Australia, 1987.
19. Cheng, W.-Q.; Rudd, M.E.; Hsu, Y.-Y. Angular and energy distributions of electrons from 7.5–150-keV proton collisions with oxygen and carbon dioxide. *Phys. Rev. A* **1989**, *40*, 3599. [CrossRef] [PubMed]
20. Bates, D.R.; Griffing, G.W. Inelastic Collisions between Heavy Particles I: Excitation and Ionization of Hydrogen Atoms in Fast Encounters with Protons and with other Hydrogen Atoms. *Proc. Phys. Soc. A* **1953**, *66*, 961. [CrossRef]
21. Hooper, J.; McDaniel, E.; Martin, D.; Harmer, D. Ionization Cross Sections for Protons on Hydrogen Gas in the Energy Range 0.15 to 1.10 MeV. *Phys. Rev.* **1961**, *121*, 1123. [CrossRef]
22. Macek, J. Theory of the Forward Peak in the Angular Distribution of Electrons Ejecteed by Fast Protons. *Phys. Rev. A* **1970**, *1*, 235. [CrossRef]
23. Galassi, M.; Rivarola, R.; Fainstein, P. Multicenter character in single-electron emission from $H_2$ molecules by ion impact. *Phys. Rev. A* **2004**, *70*, 032721. [CrossRef]
24. Plowman, C.T.; Abdurakhmanov, I.B.; Bray, I.; Kadyrov, A.S. Energy and angular distributions of electrons emitted in proton collisions with molecular hydrogen. *Phys. Rev. A* **2023**, *107*, 032824. [CrossRef]

25. Abdurakhmanov, I.B.; Kadyrov, A.S.; Bray, I. Wave-packet continuum-discretization approach to ion-atom collisions: Nonrearrangement scattering. *Phys. Rev. A* **2016**, *94*, 022703. [CrossRef]
26. Abdurakhmanov, I.B.; Kadyrov, A.S.; Avazbaev, S.K.; Bray, I. Solution of the proton-hydrogen scattering problem using a quantum-mechanical two-center convergent close-coupling method. *J. Phys. B* **2016**, *49*, 115203. [CrossRef]
27. Abdurakhmanov, I.B.; Bailey, J.J.; Kadyrov, A.S.; Bray, I. Wave-packet continuum-discretization approach to ion-atom collisions including rearrangement: Application to differential ionization in proton-hydrogen scattering. *Phys. Rev. A* **2018**, *97*, 032707. [CrossRef]
28. Plowman, C.T.; Spicer, K.H.; Abdurakhmanov, I.B.; Kadyrov, A.S.; Bray, I. Singly differential cross sections for direct scattering, electron capture, and ionization in proton-hydrogen collisions. *Phys. Rev. A* **2020**, *102*, 052810. [CrossRef]
29. Spicer, K.H.; Plowman, C.T.; Abdurakhmanov, I.B.; Alladustov, S.U.; Bray, I.; Kadyrov, A.S. Proton-helium collisions at intermediate energies: Singly differential ionization cross sections. *Phys. Rev. A* **2021**, *104*, 052815. [CrossRef]
30. Plowman, C.T.; Abdurakhmanov, I.B.; Bray, I.; Kadyrov, A.S. Differential scattering in proton collisions with molecular hydrogen. *Eur. Phys. J. D* **2022**, *76*, 129. [CrossRef]
31. Spicer, K.H.; Plowman, C.T.; Abdurakhmanov, I.B.; Kadyrov, A.S.; Bray, I.; Alladustov, S.U. Differential study of proton-helium collisions at intermediate energies: Elastic scattering, excitation, and electron capture. *Phys. Rev. A* **2021**, *104*, 032818. [CrossRef]
32. Plowman, C.T.; Abdurakhmanov, I.B.; Bray, I.; Kadyrov, A.S. Effective one-electron approach to proton collisions with molecular hydrogen. *Eur. Phys. J. D* **2022**, *76*, 31. [CrossRef]
33. Vanne, Y.V.; Saenz, A. Ionisation of $H_2$ in intense ultrashort laser pulses: Parallel versus perpendicular orientation. *J. Mod. Opt.* **2008**, *55*, 2665. [CrossRef]
34. Abdurakhmanov, I.B.; Plowman, C.T.; Kadyrov, A.S.; Bray, I.; Mukhamedzhanov, A.M. One-center close-coupling approach to two-center rearrangement collisions. *J. Phys. B* **2020**, *53*, 145201. [CrossRef]
35. Kadyrov, A.S.; Bray, I.; Mukhamedzhanov, A.M.; Stelbovics, A.T. Coulomb Breakup Problem. *Phys. Rev. Lett.* **2008**, *101*, 230405. [CrossRef] [PubMed]
36. Kadyrov, A.S.; Bray, I.; Mukhamedzhanov, A.M.; Stelbovics, A.T. Surface-integral formulation of scattering theory. *Ann. Phys.* **2009**, *324*, 1516. [CrossRef]
37. Kadyrov, A.S.; Bailey, J.J.; Bray, I.; Stelbovics, A.T. Two-center approach to fully differential positron-impact ionization of hydrogen. *Phys. Rev. A* **2014**, *89*, 012706. [CrossRef]
38. Anderson, W.L. Fast Hankel Transforms Using Related and Lagged Convolutions. *ACM Trans. Math. Softw. (TOMS)* **1982**, *8*, 344. [CrossRef]
39. Horbatsch, M. (York University, Toronto, ON, Canada) Private communication, 2023.
40. Rudd, M.E. *Phys. Rev. A* **1979**, *20*, 787. [CrossRef]
41. Alexander, J.S.; Laforge, A.C.; Hasan, A.; Machavariani, Z.S.; Ciappina, M.F.; Rivarola, R.D.; Madison, D.H.; Schulz, M. Interference effects due to projectile target nucleus scattering in single ionization of $H_2$ by 75-keV proton impact. *Phys. Rev. A* **2008**, *78*, 060701. [CrossRef]
42. Sharma, S.; Arthanayaka, T.; Hasan, A.; Lamichhane, B.; Remolina, J.; Smith, A.; Schulz, M. Complete momentum balance in ionization of $H_2$ by 75-keV-proton impact for varying projectile coherence. *Phys. Rev. A* **2014**, *89*, 052703. [CrossRef]
43. Spicer, K.H.; Plowman, C.T.; Alladustov, S.U.; Abdurakhmanov, I.B.; Bray, I.; Kadyrov, A.S. Doubly differential cross sections for ionisation in proton–Helium collisions at intermediate energies: Energy and angular distribution of emitted electrons. *Eur. Phys. J. D* **2023**, *77*, 131. [CrossRef]
44. Spicer, K.H.; Plowman, C.T.; Schulz, M.; Kadyrov, A.S. Doubly differential ionization in proton-helium collisions at intermediate energies: Energy distribution of emitted electrons as a function of scattered-projectile angle. *Phys. Rev. A* **2023**, *108*, 022803. [CrossRef]
45. Schulz, M.; Hasan, A.; Maydanyuk, N.; Foster, M.; Tooke, B.; Madison, D.H. Kinematically complete experiment on single ionization in 75-keV p + He collisions. *Phys. Rev. A* **2006**, *73*, 062704. [CrossRef]
46. Abdurakhmanov, I.B.; Kadyrov, A.S.; Bray, I.; Bartschat, K. Wave-packet continuum-discretization approach to single ionization of helium by antiprotons and energetic protons. *Phys. Rev. A* **2017**, *96*, 022702. [CrossRef]
47. Abdurakhmanov, I.; Kadyrov, A.; Alladustov, S.U.; Bray, I.; Bartschat, K. Fully differential cross sections for single ionization of helium by energetic protons. *Phys. Rev. A* **2019**, *100*, 062708. [CrossRef]
48. Gassert, H.; Chuluunbaatar, O.; Waitz, M.; Trinter, F.; Kim, H.-K.; Bauer, T.; Laucke, A.; Müller, C.; Voigtsberger, J.; Weller, M.; et al. Agreement of Experiment and Theory on the Single Ionization of Helium by Fast Proton Impact. *Phys. Rev. Lett.* **2016**, *116*, 073201. [CrossRef] [PubMed]